UNRAVELLING THE STRUCTURE OF ASPHERICAL PROTOPLANETARY NEBULAE. I. *HST* IMAGING AND OH MASER-LINE OBSERVATIONS OF ROBERTS 22

Raghvendra Sahai[1], A. Zijlstra[2], V. Bujarrabal[3], P. te Lintel Hekkert[4]

ABSTRACT

We have obtained high-resolution wide-band, narrow-band and polarimetric images of the bipolar protoplanetary nebula Roberts 22 with the Wide-Field & Planetary Camera 2 on HST. OH maser-line emission has also been observed using the Australia Telescope Compact Array. The wide-band images at 0.6μm show bright bipolar lobes shaped like a butterfly's "wings", separated by a dark equatorial "body" of dense dust which completely obscures the central star. The material within each lobe appears to be organized into an amazingly complex pattern of a very large number of intersecting loops and filaments. The bright lobes are surrounded by a fainter halo whose inner region contains multiple thin shell structures, reminiscent of those seen in the prototype protoplanetary nebula, CRL2688 (Egg Nebula). The halo can be traced to a distance of about $25''$ from the nebular center. The radial surface brightness of the halo is inconsistent with that expected for time-invariant mass-loss at a constant expansion velocity. A simple model of the radial scattered light distribution supports the hypothesis that the bright lobes are cavities with thin ($<0''5$), dense walls which are optically-thick in scattered light. The amount of mass in the cavity walls is quite large ($0.3M_\odot$) and the dynamical time-scale for their formation is short ($\lesssim 440$ yr). The bright lobes show high fractional polarisation (40-50%) and a centro-symmetric polarisation pattern, typical of a singly-scattering reflection nebula. In contrast, the polarisation in the dark equatorial region is small, and the polarisation vectors do not show a simple orientation pattern. The polarisation data has been compared with published models to set rough constraints on the dust albedo and scattering phase function and the nebular optical depths. The OH maser-line emission at 1665 and 1667 MHz is found to be concentrated in the the dark equatorial region; the kinematics of the OH features indicates that they arise in low-latitudes outflows. The nebular morphology in Roberts 22 is characterised by a high degree of point-symmetry, which may result from the interaction of collimated bipolar outflows with the progenitor AGB envelope.

Subject headings: planetary nebulae, stars: AGB and post–AGB, stars: mass–loss, circumstellar matter

[1] Jet Propulsion Laboratory, MS 183-900, California Institute of Technology, Pasadena, CA 91109

[2] UMIST, Department of Physics, PO Box 88, Manchester M60 1QD, UK

[3] Observatorio Astronómico Nacional, Ap. 1143, 28800 Alcala de Henares, Spain

[4] Australia Telescope National Facility, PO Box 76, Epping, NSW 2121, Australia

1. Introduction

Planetary Nebulae (PN) evolve from intermediate mass (1-8 $M_\odot$) stars, following a period of intensive mass loss (10^{-5}-10^{-4} $M_\odot$ yr^{-1}) during the Asymptotic Giant Branch (AGB) phase of stellar evolution. When most of the stellar envelope of the AGB star has been expelled, the hot ($T_{eff} \gtrsim 25,000$K) carbon-oxygen (white-dwarf) core is exposed, so UV radiation begins to ionize the surrounding circumstellar envelope (CSE) and a PN is formed. Multi-wavelength ground-based imaging surveys have shown that even though they evolve from mostly spherically-symmetric AGB stars, the vast majority ($\sim$ 80%) of PN deviate from spherical symmetry (e.g. Zuckerman & Aller 1986, Schwarz, Corradi, & Melnick et al. 1992, Aaquist & Kwok 1991, Kwok & Zhang 1998); a result that has been confirmed by Hubble Space Telescope (HST)/Wide Field & Planetary Camera 2 (WFPC2) imaging (Sahai & Trauger 1998, hereafter ST98).

The origin of the overall morphology of PN and their detailed structure poses a major problem for our understanding of the dynamics of PN. Since PN result from the ejected CSEs of AGB stars, PN morphologies are probably created (or drastically altered) during the evolution from the AGB to the PN stage. The current paradigm for the shaping and final morphology of PN – the generalised interacting stellar winds ("GISW") model – is that it results from the interaction between a fast radiatively-driven central-star wind with the CSE of the AGB progenitor (Kwok 1982, Balick 1987). Detailed hydrodynamical calculations confirm that many common *axisymmetric* morphologies of PN can be produced by the GISW model (e.g. Mellema & Frank 1995 and references therein). However, these models fail to explain point-symmetric and/or multipolar morphologies (e.g. ST98). ST98 suggest an alternative, but related model in which the hydrodynamic sculpting of the progenitor AGB envelope by high-velocity collimated outflows early in the post-AGB evolution is the primary mechanism for shaping PN. In order to test this and other hypotheses (e.g.Mastrodemos & Morris 1998, Morris 1990, Livio 1993, Soker 1992, Garcia-Segura 1997) for the shaping of PN we are carrying out high-sensitivity, high angular-resolution imaging of proto-PN (PPN – objects in transition between the AGB and PN phases) and young PN.

In this paper, we report our results for the PPN, Roberts 22. This object has long been known as a small ($10'' \times 4''$) bipolar reflection nebula (Roberts 1962, Sanduleak & Stephenson 1973), with a completely obscured central star ($m_R > 16$ mag), a spectral type of A2 I (i.e. $T_{eff} \approx 10,000$K) (inferred from the optical spectrum of the bipolar lobes which show scattered starlight), and time-variable OH maser emission (Allen, Hyland & Caswell 1980, hereafter AHC80). The Hα emission line (also time-variable) has wings extending to ± 450 km s^{-1}, showing the presence of a high-speed outflow. Bujarrabal & Bachiller 1991 (hereafter BB91) find CO line emission at 1.3 mm, implying the presence of a dense, extended, expanding molecular envelope.

2. Observations

The optical observations were obtained with the WFPC2/HST. Both short and long exposures were obtained in pairs, allowing us to check for and correct saturation effects (where necessary) and remove cosmic-ray events. The Planetary Camera (PC) chip (800x800 pixel^2 with a plate scale of $0\rlap{.}''0456$/pixel) was used to image Roberts 22 through a wideband filter centered at 606 nm (F606W, $< \lambda >$=593.5 nm, $\delta\lambda$=149.7 nm), and narrow-band emission-line filters (Hα, F656N and [SII], F673N). A total of 8 exposures were taken with the PC (F606W – 2×200 s & 2×400 s; F656N – 2×200 s; and F673N – 2×400 s). The three Wide-Field Cameras (WF2, WF3, WF4) (each 800x800 pixel^2 with a plate scale of $0\rlap{.}''0996$/pixel) were used for polarimetric imaging of Roberts 22 at 0.6μm, using F606W crossed with the polarisation filter set POLQ. A total of 16 exposures were taken as follows: F606W+POLQ (in WF2, WF3, & WF4) – 2×200 s & 2×400 s, and F606W only (in WF3) – 2×200 s & 2×400 s. These data yielded polarised light images at three different polarisation angles.

The images taken in cameras WF2 and WF4, with the F606W and POLQ filter set, were rotated by 90.26° (clockwise) and 90.56° (counterclockwise) respectively to orient them correctly with respect to the image in WF3. The rotation angles could be determined quite accurately using the large number of field stars present in the images. The WFPC2 Polarisation Calibrator tool was used to determine the appropriate linear combinations of these images corresponding to the Stokes parameters I, Q, and U, and thus the fractional polarisation (p) and the position angle (PA) of the polarisation vectors.

Observations of the OH lines at 1665 and 1667

MHz were carried out in June 1992 using the Australia Telescope Compact Array (ATCA). The total observing time was approximately 3 hours. The two OH lines were observed simultaneously using the same calibrator, hence position errors between the two transitions are eliminated. The angular resolution achieved is $4''$, and the rms noise in the maps of the emission is about 12 mJy.

3. Results

3.1. Optical Morphology

The F606W PC images of Roberts 22 are displayed in Figure 1. An image with low spatial frequency components suppressed in order to enhance the sharp structures is also shown in false-color (the very faint regions are coded in red, whereas the brighter regions are coded in orange and yellow). The images shows bright bipolar lobes shaped like a butterfly's "wings", separated by a dark "body" of dense dust (hereafter referred to as the equatorial region or waist) which completely obscures the central star. A dark "spur" juts out into the northern lobe, with a less-pronounced linear extension towards the west. This spur probably represents an overdense clump of dust on the near side of the northern lobe, which absorbs light from the bright lobe behind it. Within each lobe, the structure, which at first sight looks simply clumpy, on closer inspection shows organization into a very large number of intersecting loops and filaments (see Fig. 1b). The bright lobes are surrounded by a fainter halo containing multiple (about 5) thin shell structures, reminiscent of those seen in the prototype PPN, CRL2688 (Egg Nebula) (Sahai et al. 1998a, Sahai et al. 1998b). In contrast to CRL2688, where the shells are nearly spherical, the shells in Roberts 22 appear distorted into shapes which roughly follow the outline of the bright lobes. The nebular morphology is characterised by a high degree of point-symmetry: the bright lobes outline a region shaped like a parallelogram, with the lines joining its vertices intersecting in the center of the nebula. The dark equatorial waist, oriented at a position angle of 121°, is close to, but not exactly parallel to the sides of the parallelogram on each side of it. The faint halo around the bright lobes is roughly rectangular in shape (with rounded corners); its long sides are roughly orthogonal to the equatorial waist. We estimate $m_V = 13.0$ for the whole nebula. The northern (N) lobe is fainter than the southern (S) one by ≈ 0.53 magnitudes. If both lobes are intrinsically equally bright[5], then the observed difference in their brightness could result from one or both of the following two mechanisms, provided the nebular axis was oriented such that the S-lobe was nearer to us. The first mechanism is preferential attenuation by an extended overdense equatorial region, and the second is a strongly forward-throwing scattering phase function. The second mechanism appears less likely based on our polarisation data (§3.3).

The F656N and F673N images of Roberts 22 show an almost identical morphology to that seen in F606W, indicating that we are mostly seeing scattered light in both narrow-line filters. In the case of F656N, the total counts/sec are a factor 3.9-2.4 times larger than the contribution expected (based on the observed counts in the F606W image) from the scattered continuum of an A-type star and a modest reddening range of $E_{B-V} = 0$-1.5. This implies that the F656N image is dominated by Hα emission from the central emission-line star, scattered by the nebular dust. The counts in the F673N image are roughly consistent with those expected from the scattered continuum light. Thus, there is no strong optical emission-line flux which arises within the nebular lobes, consistent with the low T_{eff} of the central star which is insufficient for producing any substantial ionisation of the nebular gas. However, the collision of the high-velocity wind seen in Hα with the surrounding envelope will result in shocks which could produce weak but detectable ionisation.

In order to search for the existence of such ionised gas, we have examined the F656N/F606W and F673N/F606W ratio images (Fig. 2a & 2b, respectively). The images in Figure 2 show that the F656N/F606W and F673N/F606W ratios are roughly constant in the outer regions, but rise in the inner regions, including the dark equatorial waist, by a factor ≈ 1.6. In the absence of variable nebular extinction, pure scattering would result in a constant value for the ratio in these images. However, because of the reduced extinction in the wavelength ranges covered by the F656N and F673N filters, compared to the F606W filter, an increase in nebular extinction will produce an increase in the F656N/F606W and F673N/F606W ratios. The total nebular extinction, A_V, for scattered light at any point, P, in the nebula, is equal to the sum of the radial extinction from the star to P $[A_V(r)]$, and the

---

[5] we cannot exclude the possibility that the two lobes are intrinsically unequally bright, as e.g. the lobes of OH231.8+4.2

tangential extinction from P observed along the line-of-sight [A_V(t)]. For a radially decreasing density, A_V(r) increases with radius, whereas A_V(t) decreases with radius; hence without a detailed knowledge of the nebular density distribution it is difficult to predict how A_V varies with radius. AHC80 estimate that A_V for a typical reflected light path in Roberts 22 is $\approx$5(9.5) for a λ^{-3} (λ^{-4}) scattering law. We find that for an A-type star, the F656N/F606W and F673N/F606W ratios increase by factors of 1.2(1.6) and 1.2(1.8) for an increase in A_V of 1.5(4.5) magnitudes. Hence it is quite likely that variations in A_V account for at least some, and possibly all of the variation seen in the F656N/F606W and F673N/F606W ratio images. We conclude that our HST imaging does not provide strong evidence of emission from shocked gas in the nebular lobes of Robert 22.

3.2. OH Maser-Line Emission

The OH 1665 and 1667 MHz maser-line emission is shown overlaid on the HST F606W image in Fig. 3(a,b). Both the 1665 and the 1667 MHz emission regions are seen to be concentrated in the vicinity of the equatorial waist region, with the strongest emission coming from near the geometric center of the nebula. Since the systemic velocity of Roberts 22 lies between 0 and -6 km s^{-1} V_{lsr} (BB91,AHC80), the extreme blue-shifted emission lies north-west of the center, whereas the extreme red-shifted emission lies to the south-east. The emission bluewards of the systemic velocity is significantly stronger than the red-shifted emission, suggesting that the former includes a contribution from amplified continuum emission due to a central source (e.g. a compact HII region around the central star). There is blue-shifted 1667 MHz emission about 1″ north of the center, probably associated with the dark spur. The 1665 MHz emission is notably more compact than the 1667 MHz emission, similar to the situation in AGB envelopes, and consistent with the theoretical expectation (Field 1985) that the 1665 MHz line is emitted from higher temperature regions than the 1667 MHz line.

Although the overall spatial distribution of the OH emission is similar to that seen in the very young PN, M1-92 (Seaquist, Plume & Davis 1991) and the AGB object OH231.8+4.2 (Morris, Bowers, & Turner 1982), where it has been modelled as dominantly arising in an expanding dusty equatorial torus, the detailed spatio-kinematical structure of the OH emission in Roberts 22 does not lend itself to a similarly

simple interpretation. The OH emission blobs are distributed in a distinctly lop-sided manner around the bipolarity axis, with the blue-shifted (red-shifted) features lying, on the average, north-west (south-east) of the center. This distribution may be interpreted as arising in gas outflowing along directions whose projected orientations on the sky are spread in a modest range around the NW-SE direction. We therefore propose that in Roberts 22, the OH emission is dominantly associated with radially expanding gas at *low latitudes*, possibly in the form of multiple bipolar[6] outflows. The confinement of the OH outflows to low latitudes, together with the inferred tilt of the bipolarity axis of Robert 22 (§3.1), implies that the blue-shifted (red-shifted) OH features should lie on the northern (southern) side of the equatorial waist, consistent with the observed pattern (Fig 3a,b). The dark spur appears to be part of an outflow directed towards us, consistent with our interpretation that it is a dusty foreground structure which blocks bright parts of the northern lobe (§3.1). The production of OH in the equatorial region may be due to evaporation of water-ice mantles on grains (from increased temperatures either due to radiation or shocks) followed by photo- or shock- dissociation of H_2O. The clumpy morphology of the equatorial waist suggests that one or more fast outflow are dynamically breaking up the dense equatorial structure, which may have been less clumpy earlier in the evolution of Roberts 22. The spur may be material which was originally part of the equatorial waist.

3.3. Optical Polarisation

The polarisation images of Roberts 22 at 0.6μm are shown in Fig. 4. Figure 4a shows the polarisation vector field superimposed on a contour map of the total intensity in a 12″×12″ region covering the full nebula. The bright lobes show a relatively high fractional polarisation (with median values of 40 and 50% respectively in the N and S lobes), and a roughly centro-symmetric pattern, implying that most of the nebular brightness in these regions is singly-scattered light from the central star. In contrast, the polarisation field in the darker equatorial region between the lobes is rather complex, with the average fractional polarisation in these regions being significantly lower than in the lobes. The NW equatorial region

---

[6]meaning *oppositely-directed*, and not to be interpreted as implying alignment with the bipolarity axis of Roberts 22

has the lowest polarisation (median value ~5%); on the SE side the polarisation is higher (median value of ~10%). The polarisation vectors are not aligned along the equatorial plane. Ground-based polarimetric imaging Scarrott & Scarrott (1995) shows a centrosymmetric polarisation pattern in the bright lobes, consistent with our HST data. However, in the equatorial waist region Scarrott & Scarrott (1995) find a pattern of "parallel" vectors, inconsistent with our HST results. The "parallel" polarisation pattern is most likely an artifact which results from the low seeing-limited angular resolution of the ground-based observations in the case of bipolar reflection nebulae (Whitney & Hartmann 1993; hereafter WH93).

We compare our data to the models of scattered light in dusty envelopes published by WH93; although these have been constructed to simulate the conditions in young stellar objects, we can use them to infer rough constraints on Roberts 22. In these models, the extended density distribution is essentially spherically symmetric, and is given by $\rho(\mathrm{r}) \propto r^{-3/2}$ for $\mathrm{r} \gg \mathrm{r}_c$, where r_c is the radius of a very small, geometrically-thin, optically thick equatorial disk at the nebular center. Thus, at radii small compared to the size of the nebula, the density distribution becomes progressively more flattened. Qualitatively, to zeroth order, such a density distribution is not unlike what we envisage for Roberts 22. WH93 provide model images and polarisation maps for a large number of models, with and without bipolar cavities. Two types of grains are used: type 1 having a high albedo (ω=0.5) and a forward-throwing phase function, type 2, having a low albedo (ω=0.2) and a Rayleigh-scattering phase function.

A direct comparison of the contours defining the Roberts 22 image with the models - in particular the "pinched-in" ones defining the equatorial waist - show that only the highest inclination (i=angle between line-of-sight and bipolar symmetry axis of nebula), highest optical depth models provide qualitatively reasonable fits. Thus amongst models 1-4 (models without bipolar cavities), and models 5-10 (with bipolar cavities), only models 1,2 & 5-8, at $i = 90°$, provide good fits to the observed morphology. The models are numbered such that model within the pairs 1 & 2, 3 &4, ..., 9 & 10, are identical except that the grain albedos and phase functions belong to type 1 (2) for the odd-(even-) numbered pair. Amongst these models, the typical polarisation levels in the bipolar lobes are ≈25% for the high-albedo models (1,5,7)

and ≈50% for the low-albedo ones (2,6,8). Thus our Roberts 22 image is better matched by models with type 2 grains, i.e. 2,6,8. All models are characterised by the envelope optical depth, τ, measured along a line-of-sight to the inner radius of the envelope, as a function of the inclination angle. In models 2,6,&8, at e.g. $i = 60°$, τ is 5,11 & 3.4, respectively; for the models which do not fit, the corresponding values of τ are significantly lower ($\leq$1.6). For models 2,6,&8, the optical depth in the equatorial plane, τ, at angles $i = 84° - 90°$, lies respectively in the ranges 8.9-20, 24-50, &7.5-20 consistent with the lower limit of 16.5 which we estimate in §3.4 from our images. In contrast, the non-fitting models have equatorial optical depths which lie in the range 2.8-5, and are therefore too low. The average number of scatters in models 2,6,&8 is 1.2-1.3, i.e. close to unity, implying that the observed light is dominated by singly-scattered photons, even though the scattering medium is optically-thick.

3.4. Radial Distribution of Scattered Intensity

The singly-scattered light in the lobes can be modeled to set constraints on the radial extinction of starlight and the line-of-sight scattering optical depth, τ_{los}, as a function of radius. For an optically thin scattering nebula (i.e. $\tau_{los} < 1$), the ratio of the observed scattered light intensity (S_λ) at any point, P, to the incident stellar radiation at P, is directly proportional to τ_{los} as follows:

$$\tau_{los} = 4y\pi\phi^2 S_\lambda \frac{4\pi D^2}{L_\lambda \exp(-\tau_{ext})} \qquad (1)$$

where L_λ is the stellar radiation per unit wavelength, D is the distance to the nebula, ϕ and $\exp(-\tau_{ext})$ are, respectively, the angular distance and attenuation from the star to P. The factor y depends on the radial density distribution, and varies from unity for the case when the bulk of the scattering material along the line-of-sight is localised at P, to 2 for an inverse-square density envelope. If $\exp(-\tau_{ext})$ is negligible, then τ_{los} can be estimated using Eqn. 1, since

$$\frac{L_\lambda}{4\pi D^2} = (\frac{F_{bol}}{\sigma T_{eff}^4}) \frac{2\pi hc/\lambda^3}{\exp(hc/\lambda k T_{eff}) - 1} \qquad (2)$$

where F_{bol}, the bolometric flux, is determined from ground-based and IRAS photometry to be 2.5×10^{-7} ergs s^{-1}cm^{-2} (§4), and T$_{eff} \approx 10^4$K (§1).

In Figure 5(a), we show representative radial cuts of the 0.6μm surface brightness, $S_{0.6\mu m}$ generated from the F606W image recorded with WF3 (see §2). This image has significantly higher signal-to-noise and covers a much larger field-of-view than the F606W PC image. Each cut is 6° wide, and the mean direction of each cut is shown in Figure 1a. The cuts at high latitudes (*aa'*, *bb'*, *cc'*, *dd'*), which traverse the bright lobes, show a bright "core" region, $\theta \lesssim$(2-2''.5), where the surface brightness, $S_{0.6\mu m}$, varies rather slowly with radius, followed by a "halo" region where it first drops very rapidly out to r$\approx$7''(inner halo), and then more slowly (outer halo). Cut ee' traverses the equatorial plane, and shows a steady decrease in the intensity with radius. In Figure 5(b), we present the radial intensity averaged over a large angular range, allowing us to increase the signal-to-noise ratio in the very faint outer regions. The angular region was selected to avoid the presence of very bright field stars, which contribute a significant amount of scattered light around them. Faint stars have been "removed" from the angular regions included in the cuts by the mean nebular level obtained by interpolation across their locations. The outer halo can be seen to extend out to at least r$\approx$20'', and perhaps as far as 30'', where it becomes limited by uncertainties in the background sky level. Power-law fits ($S_{0.6\mu m} \propto r^{-\alpha}$) to the inner and outer halo gives values for α of ~4.5-6.5 and ~1-2, respectively. Since α=3 is expected for time-invariant mass-loss at a constant expansion velocity, the observed values of α in the halo could be interpreted as due to changes with time of the mass-loss rate. Such an interpretation, however, is not straightforward, since we have seen that the radial distribution of material is also peculiar in the bright core region, probably due to the effects of a strong shock interaction. Such an interaction could also have affected the halo density distribution.

At ϕ=4'' in cut *cc'*, we find $S_{0.6\mu m}$=86 μJy arcsec^{-2}. Using the above equation, with $y = 2$, and τ_{ext}=0, we get $\tau_{los} = 6.5 \times 10^{-4}$. This value is about a factor 400 lower than the values estimated from modeling the far-infrared emission (see §4), or from the mass-loss rate derived from CO data (and a typical gas-to-dust ratio). Even though the models for estimating the above mass-loss rates assume that the nebula is spherically symmetric, which it clearly is not, the discrepancy in the optical depth is much too large to be an artifact of using spherically-symmetric models. The simplest explanation is that the starlight is heav-

ily attenuated even along *near-polar directions* before reaching the nebular lobes; the attenuation required corresponds to a radial extinction optical depth of $\tau_{0,ext}$ ~6, consistent with previous results (AHC80, see §3.1) and our result from analysing the polarisation images (§3.3). We can estimate the 0.6μm radial extinction optical depth towards the star through the *equatorial waist* (τ_*) from the absence of a point source in the central region. With no dust attenuation, the type-A star would produce 7.5×10^7 e^-s^{-1} in the PC chip. We find that a conservative upper limit on a point-source at or near the nebular center is 6 e^-s^{-1}; hence $\tau_* \gtrsim$16.5.

We now develop a simple model which qualitatively explains the observed radial distribution of starlight in Roberts 22. In this and all further analysis in the paper, we assume a value of 2 kpc (as recommended by AHC80) for the distance to Roberts 22, and 30 km s^{-1} for the nebular expansion velocity (V_{exp}). We have adopted a distance smaller than that suggested by BB91 (4 kpc), because at 4 kpc, the luminosity of Roberts 22 is rather large (10^5 $L_\odot$) compared to the upper range of values found in AGB stars (~ 10^4 $L_\odot$). Although distances between 1 and 2.5 kpc are probably reasonable, we have chosen a value near the upper end of this range based on the higher than average OH expansion velocity of Roberts 22, which suggests an above-average luminosity (e.g. te Lintel Hekkert 1990). BB91 derived V_{exp}=35 km s^{-1} from their modest signal-to-noise ratio CO data, whereas the higher-quality OH line profiles shown by AHC80 suggest V_{exp}=22 km s^{-1}. The CO emission line profile extends $\approx$10 km s^{-1} redwards of the red edge of the OH profiles, and is centered $\approx$6 km s^{-1} redwards of the systemic velocity of -6 km s^{-1} V_{lsr} derived from the OH data. These discrepancies between the CO and OH profiles may be reconciled if OH emission at the most extreme red-shifted velocities, arising from the far side of the nebula, is absorbed by the same continuum central source which we think might be amplifying the blue-shifted emission (see §3.2) – the expansion velocity would then be closer to that suggested by the CO data. We conservatively adopt an intermediate value, V_{exp}=30 km s^{-1}.

For an optically-thin nebula, the surface brightness of singly-scattered photons decreases as r$^{-\alpha-1}$ for a power-law density distribution ρ(r)$\propto$ r$^{-\alpha}$. However, since the observed $S_{0.6\mu m}$ in the core region is roughly flat, then ignoring the unlikely possibility

that the density in the core region increases as r (i.e. $\alpha=-1$), we can infer the following. First, the radial extinction is *not* a strongly increasing function of radius in the core region, and second, the core is optically-thick to scattering (optically-thin walls would give the bright lobes a limb-brightened appearance, which is not observed). The first condition implies that the core contains relatively little absorbing material, i.e. it is a hollow cavity, and the second condition implies that the cavity walls have a scattering optical depth, $\tau_{w,\mathrm{sct}}$, larger than unity. The density must fall rapidly beyond the walls in order to produce the steep decrease in $S_{0.6\mu\mathrm{m}}$ observed in the halo, which must be optically-thin (since the bright lobes can be seen through it clearly). We use a simple geometrical model to test our hypothesis, and set quantitative constraints on the cavity walls and surrounding nebulosity. A schematic of this model is shown in Figure 6. The cavity wall is represented by a hemispherical shell, surrounded by a low-density hemispherical halo with $\rho(r) \propto r^{-\alpha}$. The density law inside the walls is assumed to be $\rho(r) \propto r^{-2}$. We do not *assume* in the model that the density inside the cavity is zero – we take the density to be $\rho(r) \propto r^{-2}$, and use the data to constrain it. Because the observed morphology is clearly much more complex than our model, we do not attempt a detailed fit to the data (e.g. tuning the density power-law exponents in the cavity wall and interior). Our goal here is only to demonstrate that our model can simulate reasonable approximations to (a) the variation of $S_{0.6\mu\mathrm{m}}$ in the core region and in the halo, and (b) the ratio of the brightness at nominal points within the two regions. The densities in the halo, relative to the dense walls, are constrained by the decrease in surface brightness from the inner region to the halo region.

A typical model surface brightness distribution which simulates $S_{0.6\mu\mathrm{m}}$ for cut *cc'* is shown in Figure 7(a). The model is not designed to simulate (a) the region interior to $r \lesssim 0\rlap{.}''7$ which is affected by the dense equatorial waist, or (b) the region exterior to $r \gtrsim 7''$, where the density power-law changes slope. We have assumed (i) a mean radius of $r_w=2\rlap{.}''8$ and a thickness $\delta r_w=0\rlap{.}''4$ for the wall, (ii) a halo density power-law with $\alpha \approx 6$, (iii) an isotropic dust scattering phase function, and (iv) an expansion velocity, $V_{exp}=30$ km s^{-1}. The walls have to be much denser than the cavity interior; e.g. we find that the ratio of the density in the middle of the wall to the density in the middle of the cavity (r=1$\rlap{.}''$3), R_{wi}, must be

larger than 10, in order to produce a sufficiently flat surface-brightness profile in the bright inner ($r \approx 0\rlap{.}''7$–2$\rlap{.}''5$) region. For example, Figure 7(b) shows a model with $R_{wi}=10$; clearly, the surface brightness profile in the inner region is not flat like the model in Fig. 7(a) with $R_{wi}=430$. The thickness of the cavity walls must be less than $0\rlap{.}''5$ in order to reproduce the sharp turnover of the surface brightness from the flat inner region to the steeply sloping halo region. The ratio of the density in the middle of the dense wall to that in the halo, say, at $r=4''$, is quite large (~ 100). In our models, the radial extinction optical depth from the central star to the halo region just outside the cavity walls (i.e. from O to A in Fig. 6) dominantly arises in the dense cavity walls – if we require that it equal the value estimated earlier ($\tau_{0,\mathrm{ext}} \sim 6$), then for a grain albedo of 0.3 (see §3.3), the dust density in the cavity walls is characterised by an "equivalent" dust mass-loss rate[7] of $\sim 1.2 \times 10^{-5}$ $M_\odot$ yr^{-1}, corresponding to an "equivalent" total mass-loss rate, $\dot{M}_{eq} \sim 2.4 \times 10^{-3}$ $M_\odot$ yr^{-1} for a typical gas-to-dust ratio of 200 (see §4). However, since an unknown amount of extinction may arise close to the star, this value provides an upper limit on the wall density. A lower limit on the wall density is provided by the requirement that the scattering optical depth due to the wall (i.e. along the vector BC in Fig. 6), $\tau_{w,\mathrm{sct}}$ be >1, implying $\dot{M}_{eq} > 8 \times 10^{-4}$ $M_\odot$ yr^{-1}.

Thus, $\dot{M}_{eq}$ is about an order of magnitude higher than the average mass-loss rate characterising the nebula as a whole (10^{-4} $M_\odot$ yr^{-1}, see §4), providing quantitative support for the idea that the cavity walls result from a fast wind sweeping-up matter in the slowly expanding AGB envelope into an overdense shell. Assuming that the mass-loss rate, $\dot{M}_{AGB}$, was constant in the region containing the swept-up shell (i.e. for $r< r_{out}$, where $r_{out}=$ outer radius of cavity wall) *prior to the onset of this fast wind*, then $\dot{M}_{AGB}/\dot{M}_{eq} = \delta r_w/r_{out}$. Substituting values for δr_w ($<0\rlap{.}''5$) and r_{out} (3$''$) derived from our modelling, we find $\dot{M}_{AGB} < 4 \times 10^{-4}$ $M_\odot$ yr^{-1}. The mass in the cavity walls, $(\dot{M}_{eq} \delta r_w)/V_{exp}$, is quite large, 0.3$M_\odot$ (this value is insensitive to the uncertain values of δr_w and V_{exp} because $\dot{M}_{eq} \propto V_{exp}/\delta r_w$). The dynamical time-scale for the formation of the cavity (t_{cavity}) is small. Assuming that material in the fast

---

[7] the equivalent mass-loss rate is a convenient way of representing the density, ρ, ($\dot{M}=4\pi r^2 \rho V_{exp}$) in the cavity walls, and does not represent the actual stellar mass-loss rate at any time

wind has an initial velocity of 450 km s^{-1} (from Hα data, see §1), and undergoes constant deceleration to a final velocity of 30 km s^{-1}, we find t_{cavity}=110 yr. An upper limit of 440 yr can be set on t_{cavity} by dividing the wall radius by 30 km s^{-1}.

4. The Progenitor AGB Star: Nebular Mass, Mass-Loss Rate and Luminosity

We now set constraints on the mass loss from the progenitor AGB star of Roberts 22. Some fraction of the nebular matter in Roberts 22 is readily detected in the far-infrared thermal emission from dust grains. We have therefore fitted the IRAS far-infrared fluxes of Roberts 22 to estimate the mass of warm dust, using a multi-component dust emission model (Sahai et al. 1991). The IRAS fluxes have been color-corrected according to the color temperature determined between adjacent IRAS bands (e.g. Kwok, Hrivnak & Milone 1986). A dust emissivity of 150 cm^{2}g^{-1} at 60 μm (Jura 1986), with a λ^{-p} power-law variation and p=1 and 1.5 (characteristic of amorphous grains) has been assumed. We find that the 100, 60 and 25 μm fluxes are well fit by a single warm ($\approx$100–150K) component, however the 12 μm model flux is smaller than observed. A second high temperature ($\gtrsim$500 K) component, with a mass roughly a factor $\lesssim$ 10^{-3} smaller than that of the warm component, is sufficient to make up for this deficiency. We find that the masses and temperatures of the 2 components are, respectively, 4.7(2.9)×10^{-3} and 1.2(1.4)×10^{-6} $M_\odot$ and 100(120) and 425(470) K; and the bolometric flux, is 2.6(2.3) × 10^{-7} ergs s^{-1}cm^{-2}, corresponding to a luminosity of 3.2(2.9)×10^4 $L_\odot$, for p=1.5(1). As expected, our estimate is larger than the value, 2×10^4 $L_\odot$, derived by AHC80 since the IRAS fluxes were unavailable to the the latter, and in rough agreement with the value derived by BB91.

The size of the far-infrared dust emitting region, θ_d, is unknown; if we assume that the warm dust is associated with the optical nebula seen in the F606W image, we can derive a dust ejection time-scale, $t_{exp} = (\theta_d)/(2\ V_{exp})$, which is equal to 5500 yrs with $\theta_d \approx 10''$, and V$_{exp}$=30 km s^{-1}. The progenitor AGB mass-loss rate is then estimated as $\dot{M}$=M$_d$ η/t$_{exp}$=10^{-4} $M_\odot$ yr^{-1}, where η=200, is a typical gas-to-dust ratio for AGB CSEs. We have recalculated the mass loss rate from the CO data using the model described by BB91, adjusted for our distance of 2 kpc but keeping the angular size of the

CO envelope as in BB1. The model fitting yields $\dot{M}\sim 7 \times 10^{-5}$ $M_\odot$ yr^{-1} for an assumed fractional CO abundance of 10^{-4}. The mass-loss rate from CO data is uncertain because the fractional CO abundance, the gas kinetic temperature, and the CSE size are not well determined, whereas the mass-loss rate from the IRAS data is uncertain because the dust properties, the size of the dust emitting region, and the gas-to-dust ratio are unknown. The factor $\sim$2 uncertainty in the distance also affects both mass-loss estimates. Nevertheless, in spite of these uncertainties, it is clear that the mass-loss rate for the AGB progenitor of Roberts 22 lies near the upper-end of the range (10^{-8}–10^{-4} $M_\odot$ yr^{-1}) observed for AGB stars.

5. Discussion: The Structure of Roberts 22

In the popular GISW model, aspherical PN result when a fast (1000–2000 km s^{-1}) spherical wind sweeps material in a slowly expanding progenitor AGB CSE into a thin shell, provided the CSE has an equatorial density enhancement (Balick 1987; hereafter, we will use the term "GISW model" with this restricted interpretation). This model produces bipolar shapes with reflection symmetry about the equatorial plane and cylindrical symmetry around an axis orthogonal to the equatorial plane. Hence, an object like Roberts 22, whose structure displays an overall point-symmetry, does not fit naturally into the GISW model.

Instead, Roberts 22 may fit better within the framework of the alternative two-step mechanism for the formation of PN proposed by Sahai & Trauger 1998. In this model, first, a high-speed (few 100 km s^{-1}) collimated (also referred to as jet-like) outflow (or outflows) operating during the late-AGB or early post-AGB evolutionary phase carves out an imprint within an intrinsically spherical AGB mass-loss envelope. This imprint sets the stage for the development of an aspherical PN. Subsequent expansion of a hot, tenuous, even faster stellar wind inside this imprinted AGB envelope, then produces the observed PN, whose shape and structure depends in detail on how the characteristics (direction, strength, opening angle) of the jet-like outflows change with time. The ST98 model is based on a recent Hα imaging survey of young PN, where all objects imaged showed highly aspherical morphology, with a majority characterised by multipolar bubbles distributed roughly

point-symmetrically around the central star. PN showing predominantly axi-symmetric structures are special cases of the ST98 model in which the high-speed outflow does not change its direction significantly. The notable advantage of the ST98 model over the GISW model is that it gives central importance to the role of fast, secondary outflows (with $V_{exp} \lesssim$ few$\times$100km s^{-1}) which are being found in increasing numbers in AGB stars and PPN (e.g. Sahai et al. 1991). The presence of jet-like outflows has been directly seen in many young PN and/or PN (e.g. He2-142, K3-66, & BD+30°3639: ST98; He2-104: Corradi & Schwarz 1993, MyCn18: Bryce et al. 1997, M1–92: Bujarrabal et al. 1998; NGC6543: Harrington & Borkowski 1994). Direct evidence of an imprint being carved out by a high-velocity outflow within a roughly round AGB mass-loss envelope is provided by high-resolution imaging of the prototype PPN, CRL2688 (Sahai et al. 1998a, Sahai et al. 1998b).

It is instructive to compare and contrast Roberts 22 with CRL2688 (e.g. Sahai et al. 1998a, Sahai et al. 1998b and references therein) and another well-studied PPN, the Red Rectangle (e.g. Osterbart, Langer & Weigelt 1997 and references therein). Each of these three objects is bipolar, with a pair of bright lobes separated by a dark equatorial waist, which completely obscures the central star. The spectral types of their central stars (inferred from spectra of the nebular scattered light) are also similar – A for Roberts 22 and the Red Rectangle, and F5 for CRL2688.

The detailed morphological structure of both the bipolar lobes and the waist is considerably different in Roberts 22 and CRL2688. Both nebulae show arc-like structures which are probably projections of geometrically thin shells of enhanced local density. However, in Roberts 22 only about 5 extended arcs can be seen, with shapes which are certainly not round, whereas in CRL2688 the arcs are roughly round in shape and very numerous. The shape and structure of the bright lobes in Roberts 22 is considerably more complex than that in CRL2688. The dark waist region in Roberts 22 has a considerable amount of clumpy structure, compared to the waist region in CRL2688, which is smoothly contoured. Both Roberts 22 and CRL2688 show a well-defined centro-symmetric polarisation pattern in the bipolar lobes, however in the equatorial waist region, Roberts 22, unlike CRL2688, does not show a well-defined pattern of polarisation vectors aligned parallel to the waist. Existing archival HST images of the Red Rectangle nebula do not show obvious complex clumpy structures or arc-like features.

Roberts 22 and CRL2688 have large AGB mass-loss rates, $\sim 10^{-4}$ $M_{\odot}$ yr^{-1}, and compact high-velocity outflows: in Roberts 22, the signature of this outflow is seen in the extended wings ($\pm$450 km s^{-1}) of the Hα line, whereas in CRL2688 the fast outflow is seen in the extended wings ($\pm$100 km s^{-1}) of CO rotational lines (e.g. Young et al. 1992). In contrast, only relatively narrow CO millimeter-wave line profiles in the Red Rectangle have been observed, and these have been interpreted as arising in a bipolar outflow (outflow speed of $\sim$ 7 km s^{-1}) from an edge-on disk (Jura, Balm & Kahane 1995).

Roberts 22 shows evidence for both oxygen-rich (O-rich) and carbon-rich (C-rich) circumstellar material, similar to the Red Rectangle (Waters et al. 1998), but in contrast to C-rich CRL2688. The presence of OH maser emission in Roberts 22 indicates O-rich material, whereas its infrared spectra including recent ISO-SWS spectra, show features usually associated with Polycyclic Aromatic Hydrocarbons (PAHs) which are indicative of C-rich material (Allen et al. 1982, Cohen et al. 1989, Molster et al. 1997). The far-IR ISO (23-44 μm) spectrum of Roberts 22 shows features seen in other O-rich stars (Molster et al. 1997). A favored explanation for such objects showing both C-rich and O-rich features is that the O-rich material is due to gas expelled earlier in the AGB star's mass-loss history and captured by a binary companion in a disk-like structure, whereas the C-rich material is due to gas expelled more recently after the AGB star has changed from an O-rich star to a C-rich star.

What is the origin of the bright lobes in Roberts 22? It appears to be the same as in the case of CRL2688 and M1-92, where the bright lobes are thin-walled cavities probably carved out by the hydrodynamic interaction of a fast collimated outflow expanding within the slow AGB wind (Sahai et al. 1998b, Bujarrabal et al. 1998). However, the fainter nebulosity surrounding the bright lobes in Roberts 22, which we usually associate with the progenitor AGB wind, shows large departures from circular symmetry, in contrast to CRL2688 where the nebulosity and arcs are roughly consistent with circular symmetry. Therefore, either the AGB wind in Roberts 22 was (a) intrinsically aspherical, or (b) the geometry of the slow wind in regions beyond the cavity walls has been

distorted by fast-outflow episodes which occurred before the formation of the cavities corresponding to the bright lobes. We favor hypothesis (b) in view of the large number of faint loop-like structures seen both in the bright lobes as well as the fainter surrounding nebulosity. The relatively wide CO line and the morphology evident in Fig. 1(b) also suggests that the bulk of the nebula has already suffered strong acceleration episodes, probably due to shocks. The absence of any extended shock-excited emission suggests that the gas has cooled down and that the forward shock front is now traversing a low-density region, significantly more distant from the central star than the observed bright nebulosity. Shocks may well exist in the very inner regions, but are obscured by the thick equatorial dust. They could be responsible for the $H\alpha$ excess in the scattered light.

6. Conclusions

We have obtained high-resolution wide-band, narrow-band and polarimetric images of the bipolar proto-planetary nebula Roberts 22 with the Wide-Field & Planetary Camera 2 on HST. OH maser-line emission has also been observed using the Australia Telescope Compact Array. We find that

(1) The nebula has the appearance of two bright bipolar lobes shaped like a butterfly's "wings", separated by a dark equatorial "body" of dense dust which completely obscures the central star. The material within each lobe appears to be organized into a very large number of intersecting loops and filaments. The bright lobes are surrounded by a fainter halo whose inner region contains multiple thin shell structures, reminiscent of those seen in the prototype protoplanetary nebula, CRL2688. The halo can be traced to a distance of about $25''$ from the nebular center.

(2) The scattered light in the halo first decreases rapidly, and then more slowly: power-law fits ($S \propto r^{-\alpha}$) to the inner and outer regions gives values for α of $\sim$(4.5-6.5) and $\sim$(1-2), respectively, inconsistent with the value of 3 expected for time-invariant mass-loss at a constant expansion velocity.

(3) A model of the radial scattered light distribution shows that the bright lobes are cavities with dense walls which are optically-thick in scattered light. The density in the middle of the walls (which are $<0\!\!''\!5$ thick) is at least a factor 10 higher than inside the cavity, and about a factor 100 higher than in the halo at a radius of $4''$. The amount of mass in the cavity walls is quite large, $0.3 M_\odot$, and the dynamical time-

scale for their formation is $\lesssim 440$ yr.

(4) The narrow-band images at 656 and 673 nm are very similar to the broad band ($0.6 \mu m$) image, indicating that the former also mostly show scattered light. The 656 nm image has excess counts due to $H\alpha$ emission generated close to the central star and scattered by the nebula.

(5) The bright lobes show high fractional polarisation (40-50%) and a centro-symmetric polarisation pattern, typical of a singly-scattering reflection nebula. In contrast, the polarisation in the dark equatorial region is small, and the polarisation vectors do not show a simple orientation pattern. Comparison of the polarisation data with published models shows that models in which the dust grains in the lobes have a low albedo ($\sim$0.2), a Rayleigh-scattering phase function, and large optical depths, fit the data better than models with high albedo ($\sim$0.5), a forward-throwing phase function, and low optical depths.

(6) The OH maser-line emission at 1665 and 1667 MHz is found to be concentrated in the the dark equatorial region; the kinematics of the OH features indicates that they arise in low-latitude outflows.

(7) The nebular morphology is characterised by a high degree of point-symmetry, which may result from the interaction of collimated bipolar outflows with the progenitor AGB envelope.

REFERENCES

Aaquist & Kwok 1991, ApJ, 378, 599

Allen, D.A. 1978, MNRAS, 184, 601

Allen, D.A., Hyland, A.R., & Caswell, J.L. MNRAS, 1980, 192, 505

Allen, D.A. Baines, D.W.T., Blades, J.C., & Whittet, D.C.B. MNRAS, 1982, 199, 1017

Balick, B. 1987, AJ, 94, 671

Bryce, M. Lopez, J.A., Holloway, A.J., & Meaburn, J. 1997, ApJ, 487, L161

Bujarrabal, V., Alcolea, J., Sahai, R., Zamorano, J., & Zijlstra, A.A. 1998, A&A, 331, 361

Bujarrabal, V. & Bachiller, R. 1991, A&A, 242, 247

Cohen, M., Tielens, A.G.G.M., Bregman, J., Witterborn, F.C., Rank, D.M., Allamandola, L.J., Wooden, D.H., & de Muizon, M. 1989, ApJ, 341, 246

Corradi, R.L.M. & Schwarz, H.E. 1993, A&A, 268, 714

Field, D. 1985, MNRAS, 217, 1

Garcia-Segura, G. 1997, ApJ, 489, L189

Harrington, J.P., & Borkowski, K.J. 1994, BAAS, 26, 1469

Jura, M. 1986, ApJ, 303, 327

Jura, M., Balm, S.P., & Kahane, C. 1995, ApJ, 453, 721

Kwok, S. 1982, ApJ, 258, 280

Kwok, S. & Zhang, C.Y. 1998, ApJS, 117, 341

Kwok, S., Hrivnak, B.J., & Milone, E.F. 1986, ApJ, 303, 451

Livio, M. 1993, in IAU Symposium No. 155, "Planetary Nebulae", (Kluwer Academic Publishers: Dordrecht) eds. R. Weinberger & A. Acker, pp. 279

Mastrodemos, N. and Morris, M. 1998, ApJ, 497, 303

Mellema, G. & Frank, A. 1995, MNRAS, 273, 401

Molster, F.J., Waters, L.B.F.M., de Jong, T., Prusti, T., Zijlstra, A., & Meixner, M. 1997, in *Planetary Nebulae*, IAU Symposium 180 (Kluwer Academic Publishers: Dordrecht), p361

Morris, M. 1990, in FROM MIRAS TO PLANETARY NEBULAE: Which Path for Stellar Evolution, Eds. M.O. Mennessier & A. Omont, (Editions Frontieres), p520

Morris, M., Bowers, P.F. & Turner, B.E. 1982, ApJ, 259, 625

Osterbart, R., Langer, N., & Weigelt, G. 1997, A&A, 325, 609

Roberts, M.S. 1962, AJ, 67, 79

Sahai, R., Wootten, A., Schwarz, H.E., & Clegg, R.E.S. 1991, A&A, 251, 560

Sahai, R., Hines, D.C., Kastner, J.H., Weintraub, D.A., Trauger, J.T., Rieke, M.J., Thompson, R.I., & Schneider, G. 1998a, ApJ, 492, L163

Sahai, R., et al., 1998b, ApJ, 493, 301

Sahai, R. & Trauger, J.T. 1998, AJ, 116, 1357

Sanduleak, N. & Stephenson, C.B. 1973, ApJ, 185, 899

Scarrott, S.M., & Scarrott, R.M.J. 1995, MNRAS, 277, 277

Schwarz, H.E., Corradi, R.J.M. & Melnick, J. 1992, A&AS, 96, 23

Seaquist, E.R., Plume, R., & Davis, L.E. 1992, ApJ 367, 200

Soker, N. 1992, ApJ, 389, 628

te Lintel Hekkert, 1990, PhD Thesis, University of Leiden

Waters, L.B.F.M. et al. 1998, Nature, 391, 868

Whitney, B.A. & Hartmann, L. 1993, ApJ, 402, 605

Young, K., Serabyn, G., Phillips, T.G., Knapp, G.R., Güsten, R., & Schulz, A. 1992, ApJ, 385, 265

Zuckerman, B. & Aller, L. 1986, ApJ 301, 772

Fig. 1.— Wide-band images of the protoplanetary nebula Roberts 22 taken with the PC chip (resolution $0.''0456$/pixel) of the Wide-Field & Planetary Camera 2 on the Hubble Space Telescope through the F606W filter. (a) In this reverse grey-scale image (logarithmic stretch), the maximum and minumum surface brightnesses, defining the black and white ends of the grey-scale, are 10.3 mJy arcsec^{-2} & 6.6 μJy arcsec^{-2}. The small vectors pointing to our estimated location of the central star ($\alpha_{J2000}=10^h21^m33.78^s$, $\delta_{J2000}=$-$58°05'48.''0$, marked as small-white circle in center) identify directions for the intensity cuts shown in Figure 5. (b) A false-color image generated by processing the image in (a) in order to emphasize sharp structures. The processed image, $Im_P = Im_O/(Im_O + 0.04 Im_S)$, where Im_O is the original image, and Im_S is obtained by smoothing Im_O.

Fig. 2.— (a) F656N/F606W and (b) F673N/F606W ratio images of Roberts 22. The resolution is $0.''0456$/pixel. Smaller values of the ratios are represented as darker shades in these linearly-stretched grey-scale images.

Fig. 3.— The OH 1665 and 1667 MHz maser-line emission features shown overlaid on the HST F606W image. The OH maser features have been grouped into 4 velocity bins (<-30, -30 to -10, -10 to 10, and >10 km s^{-1} V_{lsr}), and then displayed as circles with size proportional to the square-root of the integrated flux – the largest circle in panel (a) corresponds to an integrated flux of 80 Jy, and in panel (b) to 2.5 Jy.

Fig. 4.— WFPC2 polarimetric images of Roberts 22 at 0.6μm derived from exposures using the POLQ filter set in combination with F606W. The orientation of these images is the same as in Fig. 1. The images show polarisation vectors (in red) and total intensity contours (in black). A 100% polarisation vector is shown at the top of each panel. Succesive contours are spaced apart by a multiplicative factor of 1.732. In (a) the full nebula is shown with the data binned 2×2, the peak intensity contour is at 9.21 mJy arcsec^{-2}, and the 5 highest contours are labelled from 1 to 5 in order of decreasing intensity. In (b) only the inner nebular region is shown, at full resolution ($0.''0996$), the peak intensity contour is at 10.3 mJy arcsec^{-2}, and the 10 highest contours are labelled.
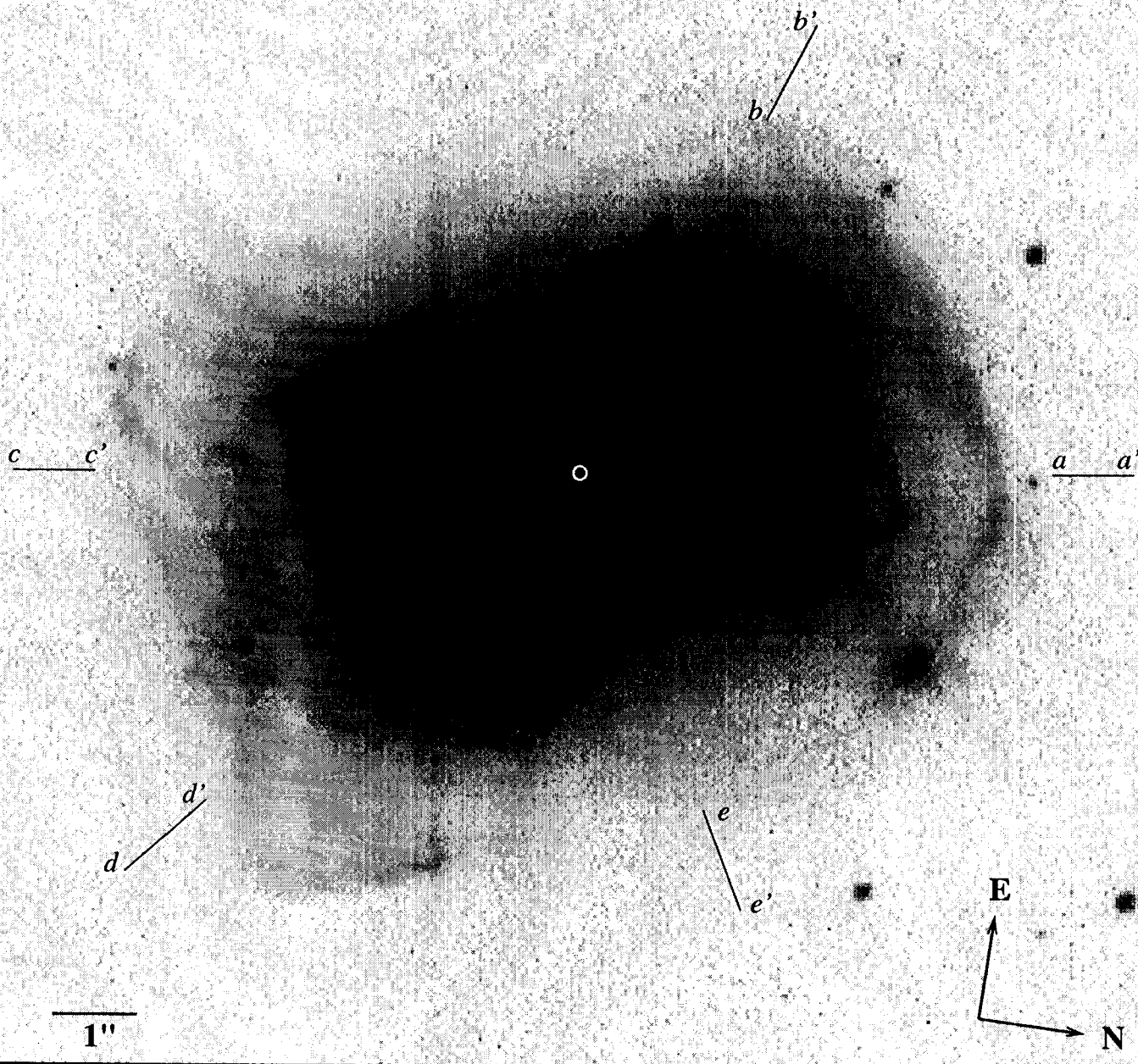
Fig. 5.— The 0.6μm continuum surface brightness as a function of radius in Roberts 22, generated by taking cuts through the F606W *HST* WF3 image along radial vectors passing through our estimated location of the central star. Panel (a) shows five different cuts (*aa'-ee'*); their directions being indicated on Figure 1(a); the cuts are 6° wide. Four of these cuts, *aa'-dd'*, correspond to different directions in the northern and southern lobes, whereas cut *ee'* traverses the dark equatorial region. The intensities for cuts *aa'-ee'* have been normalized to values of 0.206, 0.069, 5.57, 1.86, & 0.62 mJy arcsec^{-2}. Dashed lines representing the power-laws r^{-5} & r$^{-1.5}$ are also shown for comparison. Panel (b) shows the surface brightness, averaged over a 70° angular section covering the southern lobe, out to a radius of 37'', illustrating the slow decrease of the surface brightness in the outer halo region (r$\gtrsim$7''). Dashed lines representing the power-laws r^{-5} & r$^{-1.5}$ are also shown for comparison.

Fig. 6.— A schematic diagram illustrating the geometry used to model the scattered light in Roberts 22. Each of the bright lobes is represented by the hemispherical dense thin-walled cavity shown. Beyond the dense wall lies a tenuous envelope, which represents the observed halo region.

Fig. 7.— (a) The calculated 0.6μm continuum surface brightness as a function of radius in Roberts 22 which roughly simulates the observed surface brightness along cut *cc'* in Fig. 5, using the model shown in Fig. 6. The dense hemispherical cavity has a mean radius $r_w=2.''8$ & thickness $\delta r_w=0.''4$, and the low-density hemispherical halo has $\rho(r) \propto r^{-6}$. The dashed line shows an r^{-3} variation for comparison, expected for optically-thin scattering in an inverse-square density distribution. Note that the tangential scattering optical depth in the shell is significantly larger than unity, but in the halo, it is smaller than unity. (b) Same as in (a), except that the shell wall-to-interior density ratio has been reduced to 10, a factor 40 lower than that in (a), resulting in a significantly poorer fit in the inner region (r$\lesssim$2.''5).

F606W
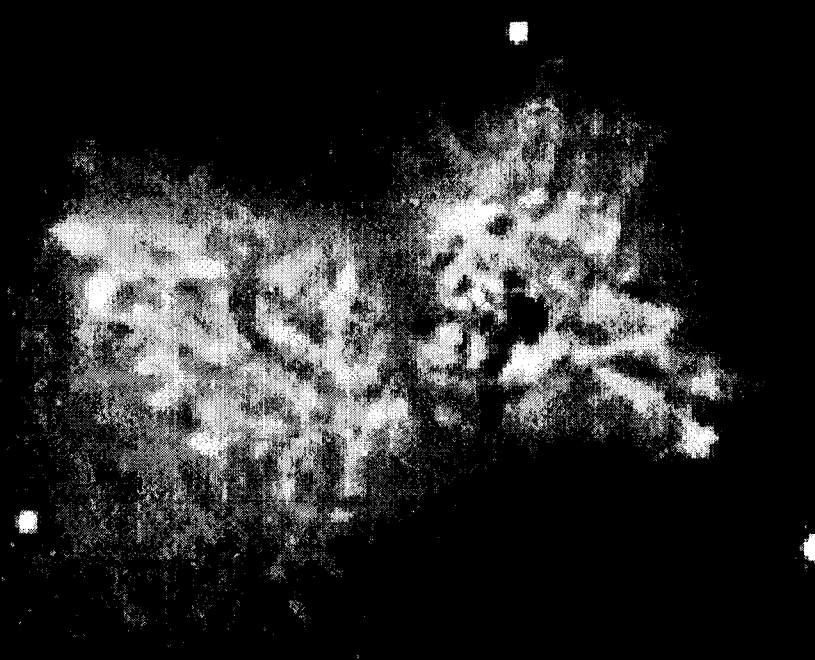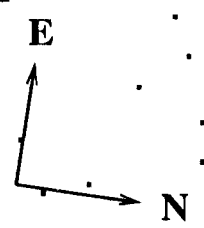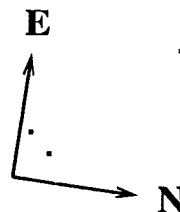
b'
b
c c'
a a'
d'
d
e
e'
1"
E
N

F656N/F606W

1"

E

N

F673N/F606W

1"

E

N

a) 1665 MHz

b) 1667 MHz

1"

1"

E

N
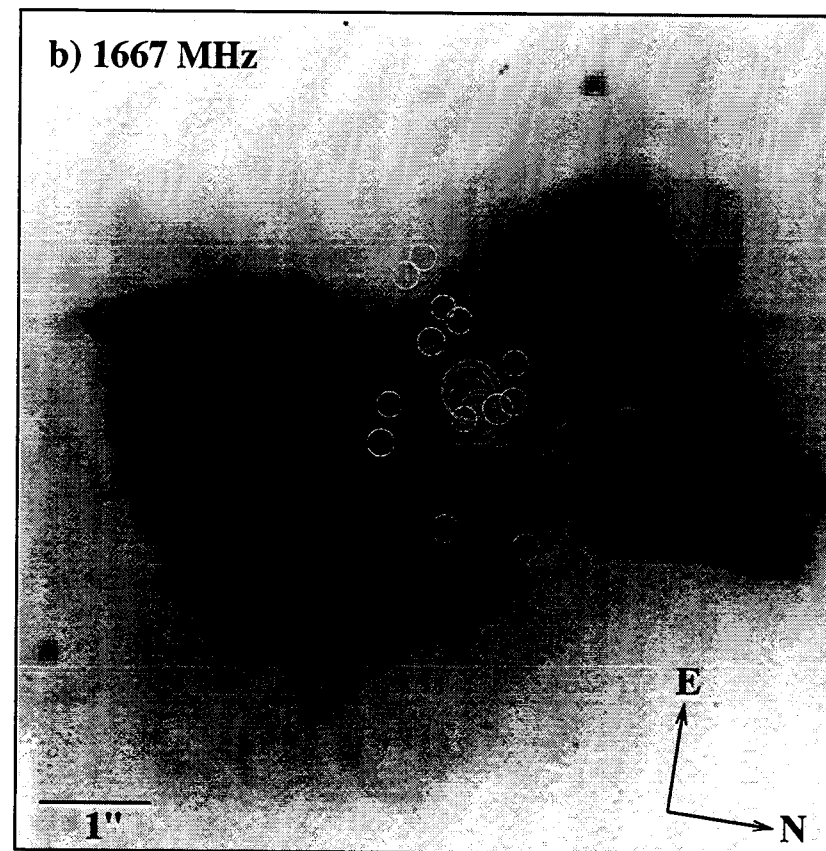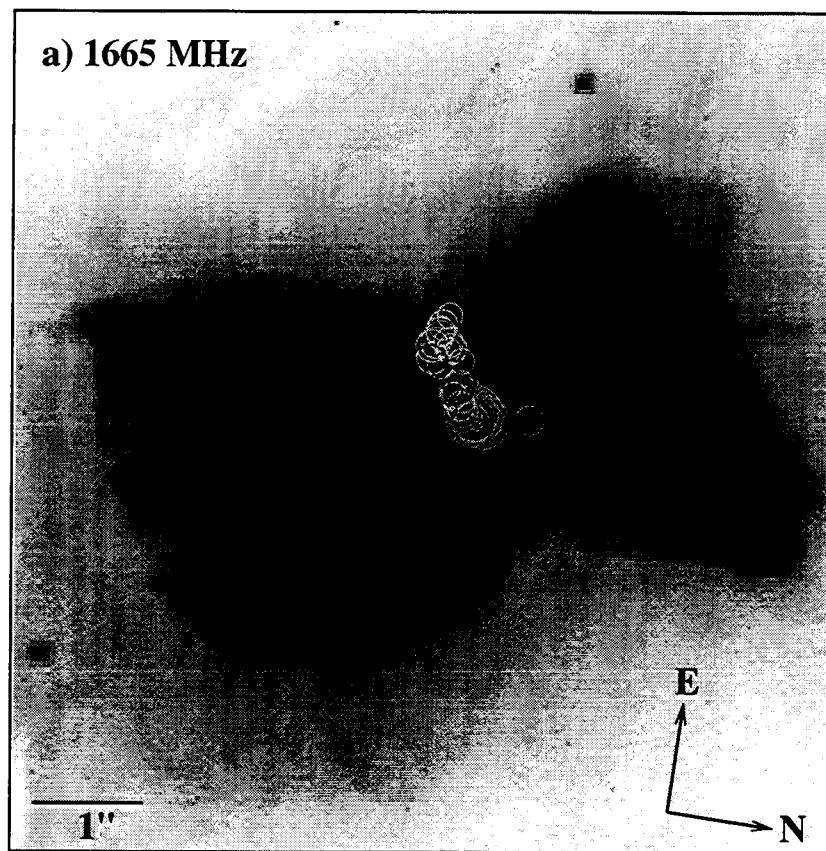
E

N
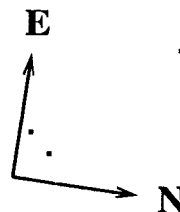
-10 < V <   10 km/s   -30 < V < -10 km/s   V < -30 km/s

$-$ 100 % polarisation

Radius (arcsec)

δr_W

B

O

A

r_W

C

wall

halo

Relative intensity vs Radius (Arcsec) — top panel labeled r^{-3}

Optical Depth vs Radius (Arcsec) — bottom panel labeled "tangential scattering optical depth" and "radial extinction"

Relative Intensity

r^{-3}

Optical Depth

tangential
scattering optical depth

radial
extinction

Radius (Arcsec)